Journal of Materials Chemistry A

Accepted Manuscript

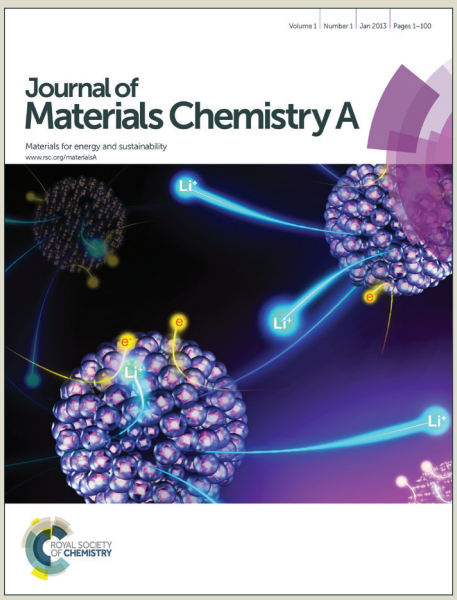

ROYAL SOCIETY OF CHEMISTRY

www.rsc.org/materialsA

Photochemical synthesis of bimetallic and anisotropic Au-containing nanoparticles using a one-step protocol

Carlos M. Gonzalez*, Benjamin Martin, Tania Betancourt

NSF-PREM Center for Interfaces in Materials
Department of Chemistry and Biochemistry, Texas State University
601 University Drive
San Marcos, TX
78666

Abstract

The production of AuAg alloys, AuAg core-shell nanoparticles, and short Au nanorods using ketyl radicals was investigated. The photochemical pair acetone/isopropanol was used as a source of reducing ketyl radicals. The process was optimized in relation to the targeted nanoparticle morphology. For every case, a simple methodology (a 1-step process) was designed aiming at the production of a particular morphology. By the simple adjustment of reagent concentrations and light intensity, the method affords nanoparticles of various compositions with a specific morphology in quantitative yield (either AuAg core-shells, or AuAg alloy nanoparticles, or Au nanorods). In addition, the plasmon properties of the colloidal systems were studied using UV spectroscopy. The mechanism of formation of each nanoparticulate system is discussed giving special attention to the factors responsible for shape and size. The role of acetone in the photochemical preparation of nanorods is further clarified. Transmission electron imaging and X-ray photoelectron spectroscopy analysis were used to characterize the colloidal nanoparticles.

Keywords: nanomaterial synthesis, photochemistry, bimetallic and anisotropic nanoparticles, plasmon spectroscopy

1. Introduction

Bimetalic and anisotropically shaped nanoparticles (NPs) offer a redefined set of advantages for catalytic, optical and electronic applications.[1-2] Such materials carry a combination of properties originating in each individual nanoparticulate element as well as a particular set of properties resulting from the more complex nanoscopic morphology and composition.[3] The most significant and attractive technological feature that such systems offers is the possibility to tune the corresponding optical and surface properties for a target application by the control of size, shape and composition. For more than a decade, the preparation and study of bimetallic and anisotropic nanoparticles have been of great interest to both the research community and industry. At present, there exist commercially available analytical platforms containing nanoparticulate metals for the detection and quantification of biological molecules. The demand for this technology is expected to grow in the near future.[4] Therefore, there is a pressing interest in the facile, low cost, and environmentally friendly synthesis of bimetallic and anisotropic nanoparticles.

AuAg alloy nanoparticles display optical properties that strongly depend on the Au-to-Ag ratio.[1-2,5-7] In particular, the corresponding plasmon band shifts from near 520 nm (Au NPs) to 400 nm (Ag NP) with an extinction coefficient that increases with Ag content. AuAg core-shell NPs display two plasmon resonances arising from the polarization of outer electrons located in two different electronic domains.[6,7] These resonances are also affected by the thickness of the deposited shell material. For example, in the case of Au(core)-Ag (shell) increasing amount of shell material shifts the plasmon-band corresponding to Au to higher frequencies and enhances the extinction coefficient. Such properties have provided the basis for the design of analytical platforms for the detection and identification of species in ultralow concentrations, *e.g*. plasmonic enhancement of single-molecule fluorescence, surface enhanced Raman scattering.[8-11] Increased catalytic performance has also been achieved through the use of bimetallic systems.[12-20] In particular, the plasmonic relaxation upon absorption of electromagnetic energy (localized surface plasmon polarization) has provided a new activation means for chemical reactions since it acts as a vehicle for the conversion of

light into chemical energy.[21-23] It is worth noting that the conversion of freely available electromagnetic radiation (sunlight) into chemical energy poses important environmental implications. In addition, the decreased content of Au in both AuAg alloy nanoparticles and core-shell structures reduces the cost of the material, which is an attractive feature for industrial investors.

In the case of anisotropically shaped metal nanoparticles, the corresponding plasmonic properties are not only dependent on intrinsic electronic features and dimension but are also dependent on the nanoparticle morphology.[24] For example, in the case of Au nanorods, the surface plasmon polarization upon interaction with UV radiation results in two distinct resonance bands. These resonances arise from the plasmon polarization of surface electrons in two directions. The oscillation of surface electrons perpendicular to the longer axes containing the nanorod results in the transverse surface resonance located in the 520-550 nm range,[25-26] and the oscillation of surface electrons along the longer axis results in the longitudinal plasmon band at variable wavelengths above 550 nm. The exact location of the longitudinal plasmon band depends on the nanorod length. In general, as the length of the main axis increases, the longitudinal resonance shifts to longer wavelengths. Similar to spherical nanoparticles, both plasmon surface polarizations are affected by changes in the dielectric constant of the surrounding media and aggregation effects.[27] Au nanorods are particularly useful for sensing platforms that are based on surface enhaced Raman spectroscopy due to slower plasmon damping dynamics and the possibility of working in the so-called optical window in biological tissue.[3,28] In this regard, the understanding of the electronic properties of this material has allowed the design of chemical and biological sensing elements, imaging reagents with enhanced performance, and photothermal therapy agents.[29-33] In the particular case of faceted rod-shaped Au nanoparticles, the presence of surface crystallographic features absent in spherical Au nanoparticles has been conveniently used in catalysis to increase reactivity and selectivity.[34-36] In addition, Au nanorods have also been employed in plasmonic catalysis.

We report a one-step photochemical process for the production of AuAg alloys, AuAg core-shell NPs, and short Au nanorods, which employs the photochemical

acetone/isopropanol system as a source of reducing 2-hydroxy-isopropyl radicals $(CH_3)_2\dot{C}-OH$ (termed ketyl radicals).[37-40] Such species result from the photochemically initiated hydrogen transfer reaction between acetone and isopropanol (as hydrogen donor) upon electronic excitation of the former (**Equations 1** and **2**).[40-42]

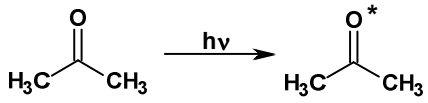

(1)

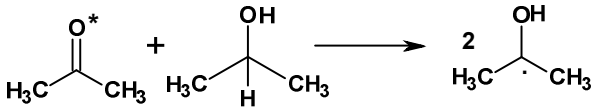

(2)

ketyl radical

The mechanism of photoreduction of ketones have been thoroughly investigated and this family of photoreactions is among the best understood of all photoreactions.[38] It is worth stressing that carbon-centered isopropanol radicals $(CH_3)_2\dot{C}-OH$ have been used before for the generation of noble metal nanoparticles.[7,43] By a simple change of reagent concentration and light intensity, the method affords nanoparticles of various composition and morphology, in quantitative yield (either core-shell or alloy nanoparticles, or Au nanorods, **Scheme 1**). In **Scheme 1**, the numbers in brackets indicate a different set of reagent concentrations, light intensity, or a combination of both. It is worth mentioning that the UV frequencies required for this work (in the UVC range) are within the range of inexpensive, mass produced UVC lamps currently used in household technologies such as furnaces with air treatment capability, surface and air sanitizing devices, and water treatment systems. Such applications are based on the germicidal character of the UVC region. This has resulted in the mass production of UVC lamps and the reduction of prices, which is a factor to consider in a scalable synthetic protocol. To the extent of our knowledge, this is the first report on the comprehensive optimization of nanoparticle morphology and composition using a single-step photochemical route. It is also the first time that the photochemical system acetone/isopropanol has been used to prepare such systems.

Scheme 1. Pictorial representation of the strategy employed for the production of bimetallic and anisotropic nanoparticles.

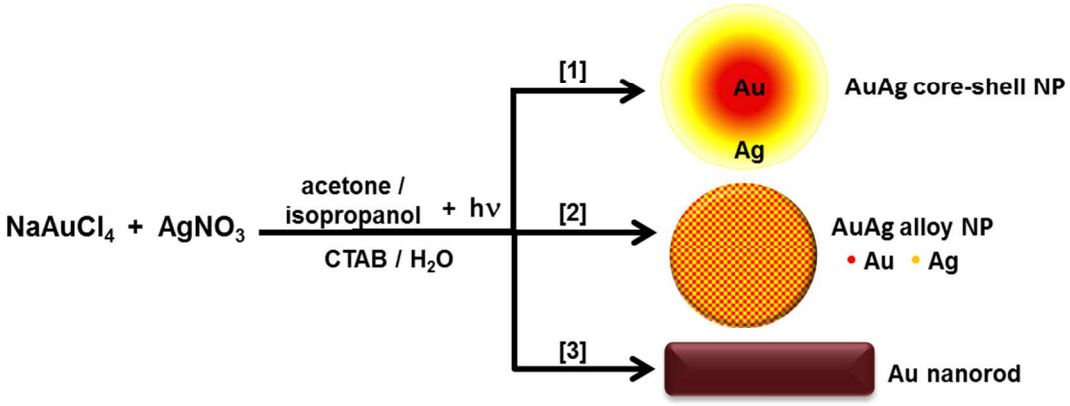

2. Experimental Part

2.1. Reagents and instruments

Sodium tetrachoroaurate, $NaAuCl_4x3H_2O$ (Sigma-Aldrich) was used as received (Sigma-Aldrich). Silver nitrate (Sigma-Aldrich) was recrystallized from ultrapure water before use. Spectroscopic grade acetone (CH_3COCH_3), spectroscopic grade isopropanol (iso-PrOH), both from Sigma-Aldrich, and hexadecyltrimethylammonium bromide (CTAB) from Fluka were used as received.

For all the experiments, a 500W Arc Lamp, model 66901 (Newport Corporation) operated at 200 W and equipped with a NewPort colored-glass (UV-filter) with band-pass in the 260-400 nm range and maximum at 280 nm was used for photolysis. Plasmon spectroscopy was recorded at 1 nm resolution, using a Synergy H4 with Hybrid Technology (BioTek), at room temperature. For kinetics monitoring, a high-resolution spectrometer HR 2000+ (Ocean Optics, range 200-600 nm) was used, coupled to a DH-2000 UV-VIS-NIR light source (Ocean Optics). The nanoparticles were also characterized by transmission electron microscopy (TEM), using a JEOL-JEM 1200 EX II at 120 kV. Scanning electron microscopy (SEM) was carried out using a FEI Helios NanoLab 400 Dual-Beam system equipped with focused ion beam technology in the 0.35 – 30 kV beam voltage range. Energy dispersive X-ray spectroscopy (EDX) was carried out to determine the elemental composition of the nanoparticles, using a 30 mm^2

silicon drift detector (SDD) with 133 eV resolution (TEAM EDX with Apollo XL SDD). The EDX system was coupled to the scanning electron microscope (FEI Helios NanoLab-400 DualBeam system equipped). For EDX analysis, the aqueous samples were placed in squared silicon wafers of approximately 1 cm^2 and allowed to dry before measurements.

2.2. Synthesis of nanoparticulate material

Bimetalic and anisotropic nanoparticles were prepared by UV irradiation (260-400 nm range, with the irradiation maximum at 280 nm) of the corresponding oxygen-purged aqueous solution containing $NaAuCl_4$, $AgNO_3$, isopropanol/acetone, and CTAB. The experiments were carried out in the 30 °C temperature range. For all the experiments, ultrapure water (18.2 MΩ cm) was used. The colloid preparations were carried out in 1 cm x 1 cm x 4 cm fused silica cuvettes. Particles with varying morphology and composition were synthesized by changing the concentration of the reagents (metal nanoparticle precursors, acetone/isopropanol and CTAB) and the light intensity, using in all cases a 1-step protocol.

For the preparation of AuAg bimetallic NPs, 3 mL aqueous solutions of total metal concentration 0.2 mM, with varying molar ratio Au-to-Ag ($[NaAuBr_4]$: $[AgNO_3]$ = 1, 0.8, 0.65, 0.5, 0.25,0), containing 25 µL of isopropanol (0.1 M), 25 µL of acetone (0.1 M) and 5 mM CTAB were irradiated with UV light (260-400 nm range). The solutions were kept at 30 °C prior to irradiation to prevent precipitation of CTAB. For the production of alloys, the light intensity used was 300 fc, and for core-shells, 75 fc. The formation of the target material was followed by the time evolution of the corresponding plasmon band.

A sample of AuAg core-shell NPs with Au-to-Ag ratio equal to 1 was prepared using Au NPs seeds. The seeds were prepared upon UV irradiation (75 fc) using a 3 mL sample containing 0.2 mM of $NaAuCl_4$, 5 mM CTAB, and 25 µL of both isopropanol (0.1 M) and acetone (0.1 M). As expected UV irradiation resulted in the formation of the characteristic red colloid. Next, a 1.5 mL sample of the Au NPs colloid was added to 1.5 mL of aqueous $AgNO_3$ (0.2 mM) in 5 mM CTAB, resulting in a system with $[AgNO_3]$ = 0.1 mM and [Au NPs]= 0.1 mM (as total Au atom concentration). Finally, 12 µL of acetone and of isopropanol were added (resulting in a final concentration 50 mM for

each). The resulting system was irradiated with UV light (260-400 nm range, 75 fc), and the process was monitored by plasmon spectroscopy.

Short Au nanorods with varying aspect ratios were prepared by UV irradiation (75 fc) of aqueous solutions (3 mL) containing 0.5 mM $NaAuCl_4$, 0.1 M CTAB, 20 mM of both acetone and isopropanol, and varying concentration of $AgNO_3$ ([$AgNO_3$] = 30, 60 and 100 μM). The intensity of the light used was in 250 fc range (260-400 nm range). The process was monitored by plasmon spectroscopy, using the growth of the transversal band to observe the progress of the process. The temperature was kept in the 30 °C range to prevent the precipitation of CTAB. The irradiation time was 30 minutes for every preparation.

Table 1 lists the concentration of reagent and light intensity employed for every target.

Table 1. Reagent concentration and light intensity used for the production of the target materials.

[Reagent] / target material	[metal] (mM)	[acetone] [isopropanol] (mM)	Irradiation Intensity (fc)	[CTAB] (mM)
alloy	0.2	100	300	5
core-shell structure	0.2	100	75	5
rod	0.5	20	250	100

3. Results and discussion

3.1. Photochemical preparation of AuAg alloy nanoparticles

AuAg alloy nanoparticles were produced by irradiating micellar solutions ([CTAB] = 5 mM) containing varying molar ratios of Au and Ag species (total concentration [$NaAuCl_4$] + [Ag^+] = 0.2 mM) with UV light (intensity 300 fc). The concentration of acetone/isopropanol was optimized to guarantee the quantitative formation of alloy nanoparticles using the available UV radiation source. The aqueous solutions were kept in the 30 °C range to prevent the precipitation of CTAB and increase the solubility of AgBr. The concentration of CTAB was optimized to minimize the formation of insoluble AgBr while promoting nanoparticle stability.

Figure 1 shows the electronic spectra for representative AuAg alloy colloids with varying composition (molar fraction for Au, χ = 1, 0.8, 0.65, 0.50, 0.25, 0). The plot shows a set of plasmon bands with a single absorption maximum. The absorption maxima consistently shift to higher energy with Ag content. The presence of a single resonance band is indicative of the formation of alloy nanoparticles.[1-2,6-7] In this regard, it has been established that Au and Ag forms stable alloys in every Au-to-Ag ratio.[6] The formation of metal solid solutions for all Au and Ag ratios has been linked to their similar crystal structures (both form pure solids with fcc unit cells and both have similar lattice constants, for Au $\rightarrow$ *a* = 4.078 Å, for Ag$\rightarrow$ *a* = 4.086 Å).[45] The sample preparation was replicated for χ(Au) = 0.8, 0.5, and 0.25. Satisfactory reproducibility was achieved. As expected, both the position and extinction coefficient of the plasmon bands depend on the corresponding Au-to-Ag molar ratio.[1-2,5-7] The plasmon maximum frequency of each alloy system, **Figure 1**, matches reasonably well the range of frequencies reported in the literature.[7,45] This strongly supports the successful formation of alloy nanoparticles by this synthetic strategy. The estimation of extinction coefficient for each alloy formulation, **Figure 2**, and further comparison with those previously reported in the literature (both experimental and calculations) suggests that the process under discussion yields alloy nanoparticles in stoichiometric amounts.[5,44] For comparative purposes, the spectra in **Figure 1** were compared with the corresponding spectra of a mixture of Au NPs and Ag NPs with matching composition, **Figure 2**. The Au and Ag nanoparticles in the mixtures were independently prepared using the procedure employed for the preparation of alloys (**Section 2.2**). The first noticeable difference was that the spectrum of each mixture of pure nanoparticles shows two distinguishable absorption maxima (with maxima at 400 and 520 nm), whose relative intensities depend on the ratio of the component single metal nanoparticles. Such absorption maxima remain centered at the position of the corresponding maximum of each monometallic colloid. These observations contrast with the presence of a single absorption band for the AuAg alloy systems, **Figure 1**.

Figure 1. Electronic spectra of a set of representiative AuAg alloy nanoparticles (χ(Au) = 1, 0.8, 0.65, 0.50, 0.25, 0). The samples were prepared with a total metal ionic form 0.2 mM, acetone/isopropanol both 0.1 M, and [CTAB] 5 mM.

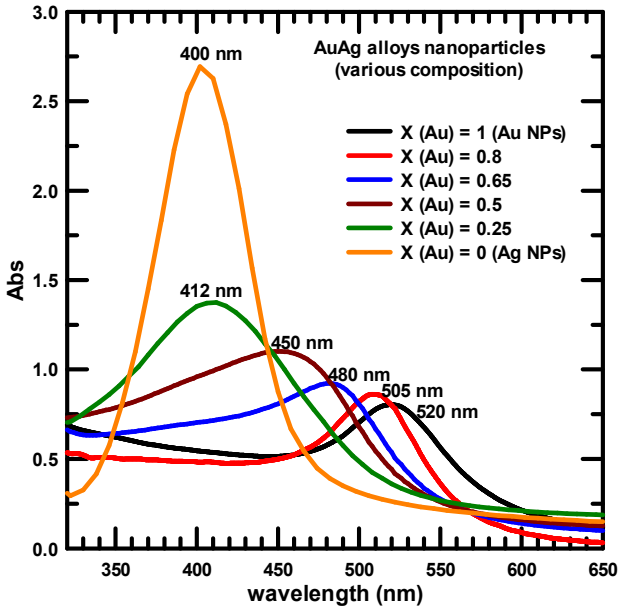

Figure 2. Electronic spectra of colloidal systems composed by mixtures of Au NPs and Ag NPs independently prepared. The samples were prepared with similar Au-to-Ag ratio as that of the bimetallic sytstem under discussion.

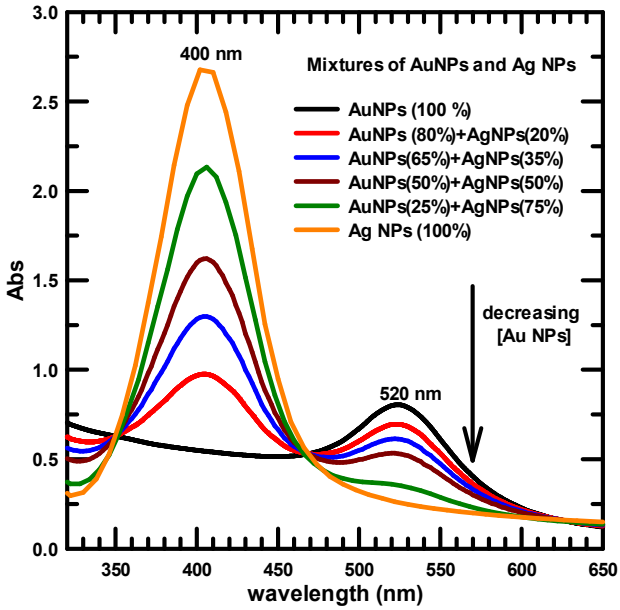

Figure 3 shows the TEM image for a representative AuAg alloy material. For this preparation, the ratio of ionic precursors $AuCl_4^-$-to- Ag^+ was 1. TEM imaging shows a majority of faceted nanoparticles with a mean population 9 ± 3 nm, and a size distribution in the 4-17 nm range (Histogram, **Figure S1**, Supporting Information). The relatively small size of the resulting nanoparticles is indicative of a high rate of seed formation triggered by the high concentration of reducing species arising from the excess of acetone/isopropanol in combination with the light intensity utilized. This situation requires the further distribution of the available material among a higher number of nucleation centers, which logically results in smaller nanoparticles. The corresponding EDX analysis of this colloid resulted in a composition with 56 % Ag and 44 % Au (over 6 determinations) in close agreement with the ratio used (1-to-1).

Figure 3. TEM image for a representative AuAg alloy nanomaterial prepared with an equimolecular Au-to-Ag molar ratio.

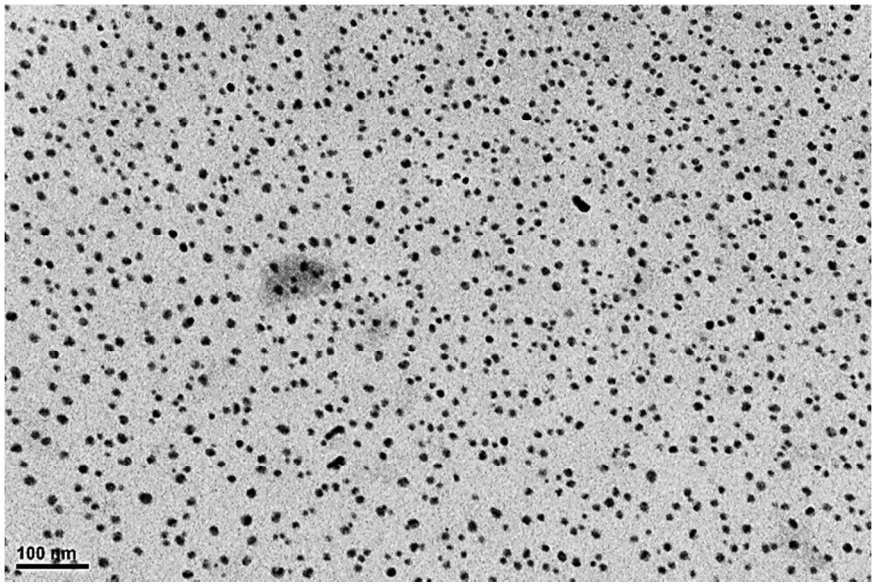

Scheme 2 shows the proposed model of the reaction dynamics responsible for the formation of bimetallic nanoparticles, including AuAg alloys. The sequence of reactions has been simplified. It is worth mentioning that the reduction of $AuCl_4^-$ occurs through the successive reduction of gold chloride species, and involves the disproportionation of Au (II).[46-47] The parallel reduction of both $AuCl_4^-$ and Ag^+

(**Equations 3** and **4**) was expected to occur due to the formation of an excess of ketyl radicals promoted by both irradiation with light in the 300 fc range, and the use of an optimal concentration of both isopropanol and acetone (both 0.1 M). As previously mentioned, the reducing ketyl radicals arise from the photochemically initiated hydrogen transfer process upon electronic excitation of acetone in the presence of isopropanol (**Equation 1-2**). [39-40] The use of either lower light intensity or lower concentration of acetone/isopropanol resulted in the splitting of the electronic spectra into two distinct absorption bands, an observation not consistent with the formation of alloy nanomaterials.[1-2,6-7] Given the electron scavenger character of both Au and Ag nanoparticles, the interaction of ketyl radicals with Au_nAg_m species (Au_nAg_m represents both bimetallic clusters and nanoparticles) should be considered (**Equation 5**), especially in a situation where unstable reducing species are in excess, which implies that negative charges are readily available.[6,48-50] The interaction results in the formation of negatively charged $(Au_nAg_m)^-$ species (**Equation 5**) and the quenching of highly energetic ketyl radicals. In this situation, the kinetics of alloy formation could be further enhanced by an autocatalytic process, in which $(Au_nAg_m)^-$ species cooperatively transfer electrons to ionic species. The formation of some insoluble AgBr does not seem to affect the formation of the target material at the optimized irradiation level. In fact, the slight cloudiness rapidly disappears within 30 seconds of irradiation. The exchange between chloride anions from $AuCl_4^-$ and bromide anions arising from the dissociation of CTAB does not seem to occur to a detectable extent in the period elapsed before photolysis. However, the exchange will progressively occur in time if the system is allowed to stand longer than 8 hours (which is evidenced by the growth of an absorption band around 380 nm, characteristic of $AuBr_4^-$).

Scheme 2. Sequence of reactions showing the basic dynamics for the formation of bimetallic nanoparticles.

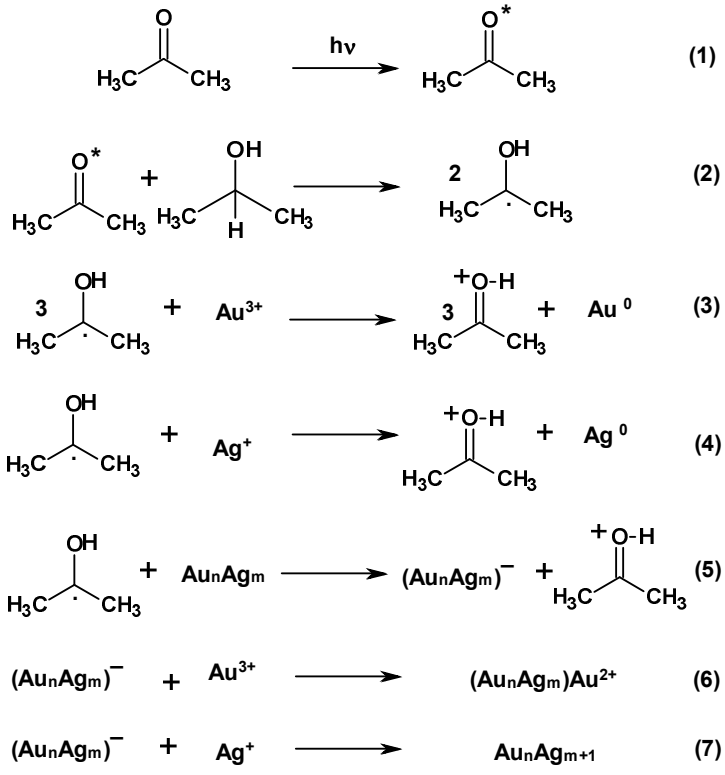

Figure 4 shows the evolution of the resonance band with cumulative irradiation periods for an alloy system prepared with an equimolecular mixture of both $AuCl_4^-$ and Ag^+. The photolysis was briefly stopped to record the evolution of electronic spectra with time. This could have promoted some electrochemical displacement reaction between alloyed Ag^0 and Au chloride species, both having been absorbed in the material surface and in solution. **Figure 4** reveals that since the earliest stages of the nanoparticle formation, the alloying process was the primary outcome, which is evidenced by the presence of a single absorption band initially centered at 488 nm (2 minute irradiation). This initial wavelength maximum (which is red-shifted with respect to the final value λ=468 nm) suggests the existence of some competition between Au(III) and Ag (I) for the available reducing species during the early photolysis period, before an optimal concentration of ketyl radical is reached. However, other factors, such as a variation in the dielectric parameters of the medium as the photolysis progresses, will have an influence on the position of the resonance band.[6] Once the concentration of ketyl

radicals has surpassed the equivalent concentration of nanoparticle ionic precursors, the parallel reduction of both $AuCl_4^-$ and Ag^+ takes place because, in this situation, the system is controlled by kinetics parameters, rather than by the order of electrochemical potential of the species involved.

Figure 4. Change in the electronic spectra with cumulative irradiation periods for an alloy system prepared with an equimolecular mixture of both $AuCl_4^-$ and Ag^+ with total concentration of 0.2 mM.

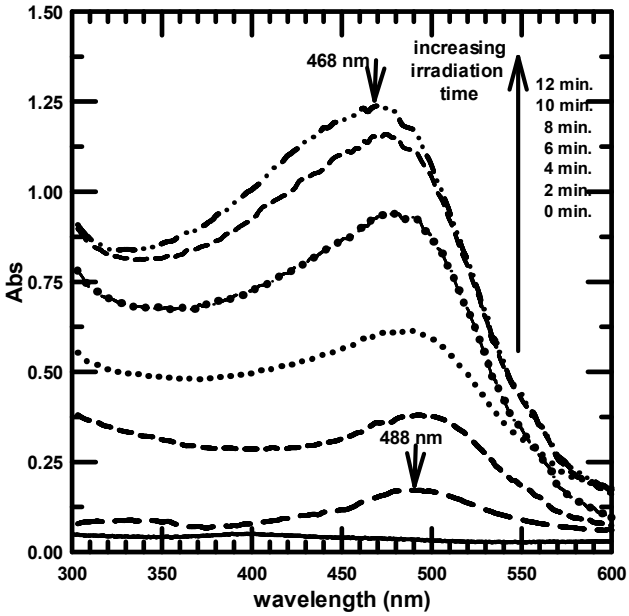

3.2. Photochemical preparation of Au(core)Ag(shell) nanoparticles

For the preparation of core-shell nanoparticles, a similar experimental setting was used as that for the AuAg alloys. The same concentration of ionic precursors, surfactants, isopropanol and acetone were employed. The light intensity was the sole experimental parameter varied to trigger the formation of core-shells.

Figure 5 shows the plasmon bands of a set of representative Au(core)Ag(shell) colloids (χ(Au)=1, 0.8, 0.65, 0.50, 0.25, 0) prepared in a single reaction step. The preparations were successfully replicated for colloids of intermediate compositions (χ(Au)= 0.8, 0.65, 0.50) and reproduced 3 times for a AuAg core-shell colloid with equimolecular metal composition. The success of this method lays in the use of UV

radiation with a lower intensity (75 fc) than the one used for the production of alloy nanoparticles (300 fc). The formation of core-shell structures was evidenced by the presence of two absorption maxima located in the proximity of the absorption range of pure Au (~ 500 nm range) and pure Ag NPs (~ 400 nm range).[1,6-7,51-54] This is more obvious for Au(core)Ag(shell) colloids with intermediate composition, *e.g.* plasmon bands in **Figure 5** for colloidal samples with 50 and 65% of Au. For nanoparticles with a larger amount of a particular metal, the spectrum shows a single absorption maximum, shifted with respect to the monometallic colloid absorption profile (**Figure 1**). Note in **Figure 5** that the plasmon bands spanning from 520 to 480 nm (reasonably assigned to Au core) have progressively shifted to the blue with increasing Ag content. This observation agrees with the literature, and is primarily related to the increased thickness of the Ag layer as more material is deposited onto the nanoparticle surface. In this situation, the Ag shell exerts a greater attraction over the outermost electron of the Au core than the stabilizing ligands bounded to the surface of pure colloidal Au nanoparticles. Consequently, interlayer electronic coupling leads to an increase in the energy required for the plasmonic oscillation of the Au valence electrons under the electromagnetic influence of the surrounding silver material.[7] The absorption profiles for the as-prepared core-shells are comparable to those previously reported in the literature.[1,6-7, 51-55] The spectra in **Figure 5** were also compared to those of a set of mixed Au and Ag NPs independently prepared (**Figure 2**). As previously mentioned (**Section 3.1**), the corresponding absorption maxima for each mixed system do not shift from the resonance maxima of each pure colloid, and the relative intensity is proportional to the ratio of material used. In contrast, for the case of core-shell systems, the absorbance corresponding to the Au core resulted progressively enhanced with Ag content (when Au content decreased) and progressively shifted to the blue. In the case of the resonance arising from the Ag shell, the corresponding band showed a progressive red-shift with increasing Au concentration. These observations indicate that the presence of two resonances in the spectra is not the result of mixed systems composed of Au and Ag NPs. For comparative purposes, **Figure 5b** shows the UV spectra for AuAg bimetallic systems with equimolecular composition (AuAg alloy NPs, AuAg core-shell NPs, and the corresponding mixture of single metal colloids).

Figure 5. **a)** Electronic spectra of a set of representiative 0.2 mM Au(core)Ag(shell) nanoparticles with varying composition prepared using photochemically generated ketyl radicals in water (5 mM CTAB). **b**) UV spectra for bimetallic systems (mixture of pure colloids, alloys and core-shell NPs) with total metal concentration 0.2 mM.

a)

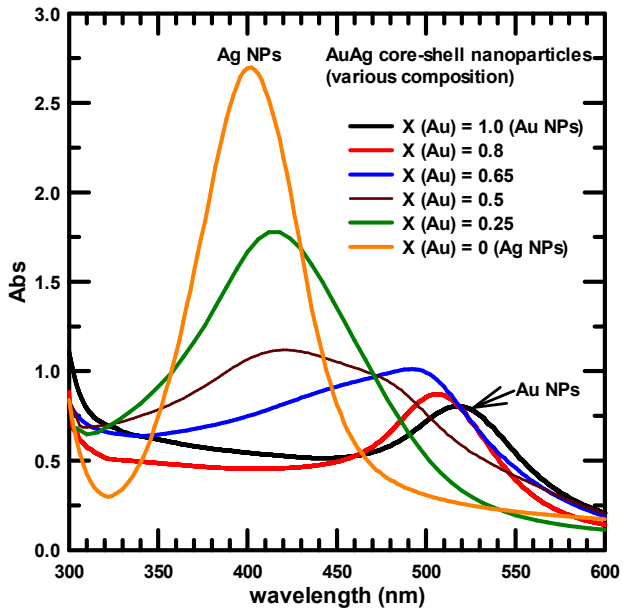

b)

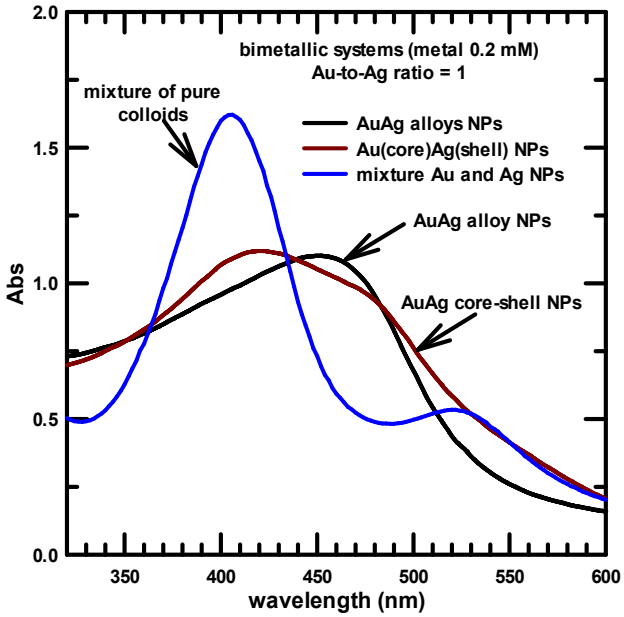

Figure 6a-c shows TEM images of Au(core)Ag(shell) NPs prepared with varying Au-to-Ag ratios. This method affords NPs with sizes in the 10-20 nm range. A histogram for the case AuAg core-shell of equimolecular composition may be found in **Figure S3**, Supplementary Information. The TEM images display the expected contrast for core-shell nanoparticles, where the darker center (higher electron density) corresponds to Au. Notice the increasing area of lighter shell with Ag content (arising from ionic Ag^{+}). In some cases, the core-shell structure is not concentric but rather shows an egg-shaped structure. For an equimolecular AuAg core-shell colloid, the EDX measurements were taken. An average atomic composition with Au ratio 49 % was obtained. As expected, this is in good agreement with the ratio of ionic precursors used for the preparation of bimetallic colloids.

Figure 6. TEM images for a sample of Au(core)Ag(shell) with varying composition, a. χ (Au) = 0.80, b. χ (Au) = 0.5, c. χ (Au) = 0.25.

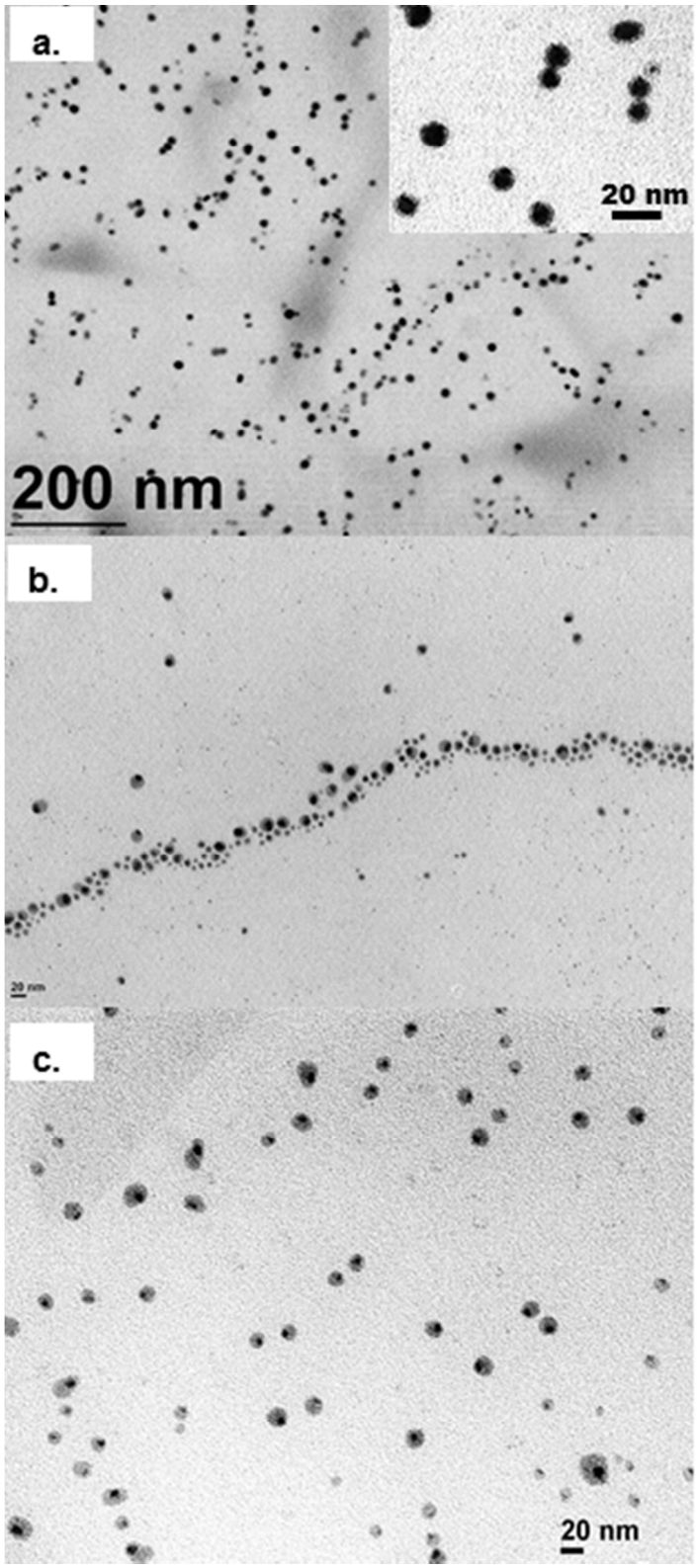

The strategy used for the formation of core-shell structures targets the slow and progressive formation of reducing ketyl radicals $(CH_3)_2\dot{C}-OH$ with irradiation so that the thermodynamic forces, defined by the electrochemical potentials, fully control the outcome of the process. In this situation, gold chloride species will reduce first, given the more positive value of the corresponding reduction potential. In cases were Ag^+ is the majority species, any successful reductive interaction between Ag^+ species and ketyl radicals will be reversed by the electrochemical displacement reaction between Ag^0 and Au chloride species. In order to further validate this strategy, the formation of Au(core)Ag(shell) NPs was monitored using plasmon spectroscopy. **Figure 7** shows the evolution of the absorption profile with cumulative irradiation time for a sample containing an equimolecular mixture of Au and Ag ionic precursors. In a first stage, the plot shows the progressive growth of a band centered at 520 nm, which is indicative of the formation of Au nanoparticles (core). In support of this statement, the extinction coefficient for this absorption band was calculated considering the full transformation of the available Au ionic precursor into nanoparticulate Au, $\varepsilon = 3.964\ 10^3\ M^{-1}cm^{-1}$. This value was compared with the calculated ε for the plasmon band of Au colloid in **Figure 5a.** For this resonance, the calculated $\varepsilon = 4.010\ 10^3\ M^{-1}cm^{-1}$. Furthermore, both of the estimated values for ε are in agreement with values reported in the literature for aqueous Au colloids of comparable size (diameter < 20 nm).[5,7] This agreement indicates that the ionic Au available for the production of Au(core)Ag(shell) was quantitatively transformed to nanoparticulate Au in the initial photolysis stage and that, under this set of conditions, an alloying process did not compete with the formation of core-shell structures. After 12 minutes of photolysis, the absorption band increased the bandwidth and progressively shifted to higher energy values, an effect which, as previously mentioned, is the result of the increasing thickness of the Ag shell. The formation of the Ag shell is evidenced by the progressive growth of band in the 415-430 nm range. Based on the plasmon spectroscopy observations (**Figure 7**), the strategy designed to trigger the formation of core-shell structures was successful. A similar progress in the spectral features was observed for all of the as-prepared Au(core)Ag(shell) colloid systems (**Figure 5a**), independently of the used ionic ratio of metal species (that is, the formation of Au 'seeds' at the first stage of the process). It is worth mentioning that the

formation of insoluble AgBr could be a contributing factor in achieving core-shell morphology, since it will result in the separation of Au and Ag species in two phases. However, it was observed that it is only at low ketyl radical concentration (resulting from the use of a low UV radiation intensity) that the low solubility of AgBr becomes a reinforcing factor. For all of the as-prepared systems, the time required to complete photolysis was ~ 40-50 minutes.

Figure 7. Change in the UV spectra with cumulative irradiation periods (at 75 fc) for a Au(core)Ag(shell) colloidal system prepared with an equimolecular mixture of both $AuCl_4^-$ and Ag^+ (total metal concentration of 0.2 mM).

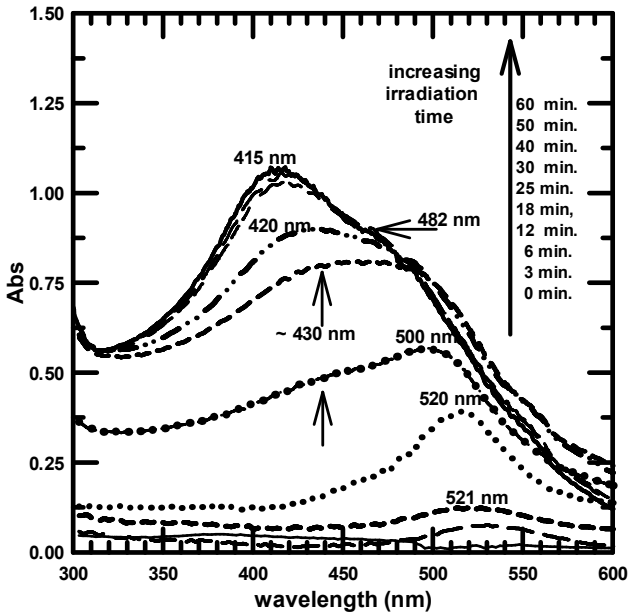

In order to further establish the effect of an increasingly denser shell of Ag on the absorption profile of these nanostructures and, in particular, on the plasmonic properties of the Au domain, the formation of AuAg core-shell NPs was monitored using Au NPs as seeds (0.1 mM), with further photoreduction of $AgNO_3$ (0.1 mM). **Figure 8** shows the growth of a second absorption maximum (indicated with vertical arrows) upon UV irradiation of a sample containing Au NP seeds and $AgNO_3$ species. Note that as photolysis progressed, the plasmon band at the lower energy range (corresponding, initially to the Au seeds) consistently shifted to higher energy values (from 520 to 482 nm), and, progressively increased intensity. A component of this enhancement should

be caused by the overlapping effect of the Ag shell. The latter observation agrees with the effect of increasingly thicker Ag shells on the resonance of the Au core material for the *in-situ* preparation of core-shell nanoparticles described previously (**Figure 7**). This simple experiment also supports the formation of core-shell structures using the protocol outlined above (the 1-step method for the preparation of AuAg core-shell NPs using ionic species, $AuCl_4^-$ and Ag^+). The spectral changes with cumulative irradiation time are not identical in both cases but are comparable. This could be linked to the different chemical environment in the two experiments. For example, in the *in-situ* preparation (1-step method), **Figure 7**, a parallel galvanic replacement step (*e.g.* $Ag^0 + AuCl_4^- \rightarrow AuCl_2 + AgCl + Cl^-$) should be important since both Ag^+ and $AuCl_4^-$ are in equal abundance. In this situation, the probability of interaction of both ionic species with reducing ketyl radical is in theory equal. Therefore, Ag^0 should form in presence of Au ionic species (which, in addition, requires further reductive steps to produce Au^0). This process is not present when the core-shell structures are produced using Au 'seeds' (**Figure 8**). Other factors such as a difference of Au core average size afforded by each method and difference in the dielectric medium could also play a role in these differences.

Figure 8. Plasmon spectroscopy monitoring the formation of Au(core)Ag(shell) NPs (molar ratio 1-to-1) using Au NPs as seeds (0.1 mM) with further photoreduction of $AgNO_3$ (0.1 mM).

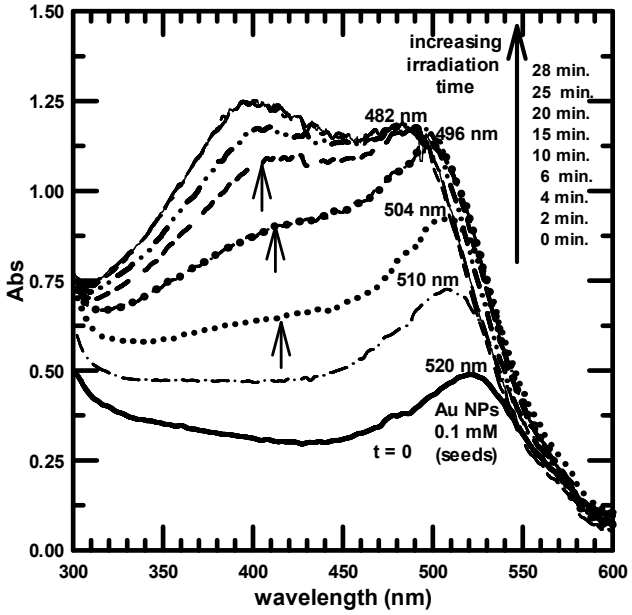

3.3. Photochemical preparation of short Au nanorods with varying aspect ratio

Au nanorods with aspect ratios 1.9, 3.0, and 3.9 were produced by irradiating (UV light, 260 - 400 nm range, intensity 250 fc) micellar solutions ([CTAB] = 0.1 M) containing 0.5 mM $NaAuCl_4$, acetone/isopropanol (20 mM each) and varying amounts of $AgNO_3$ (33, 55 and 100 μM). The aqueous solutions were kept in the 30 °C range to prevent the precipitation of CTAB. For the case under discussion, the reduction of Au species seems to proceed through gold bromide species (*e.g.* $AuBr_4^-$, AuBr) rather than through $AuCl_4^-$. This observation is based on the darkening of a 0.5 mM $NaAuCl_4$ solution upon mixing with CTAB (0.1 M), and on the parallel growth of an absorption band with maximum at ~ 390 nm, characteristic of gold bromide coordination compounds (*e.g.* $AuBr_4^-$).[47] The formation of Au nanorods was monitored using the growth of the transversal resonance with time. The irradiation time was in all cases 30 minutes. **Figure 9** shows the plasmon spectra of the as-prepared Au nanorods. The plots display the expected red-shift of the transversal resonance with increasing amount

of Ag^+ (which is related to the lengthening of the transversal axes).[56-60] The optimization of reagent concentrations and light intensity resulted in highly satisfactory reproducibility.

Figure 9. Electronic spectra of a set of Au nanorods (0.5 mM) in CTAB (0.1 M) prepared in presence of varying [Ag^+] ([Ag^+] = 33, 55 and 100 μM), using the photochemical acetone/isopropanol system.

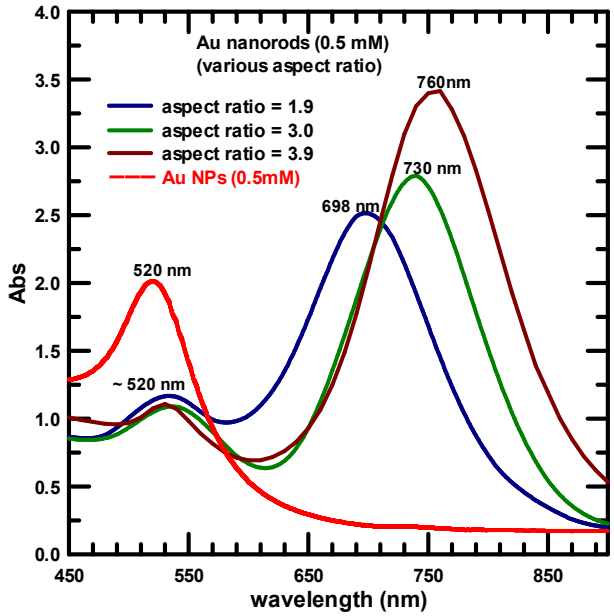

Figure 10 shows a collage with micrographs of the as-prepared Au nanorods with varying aspect ratio (AR), with the corresponding histograms. TEM imaging corroborated the effect of an increasing amount of $AgNO_3$ on the aspect ratio. The estimated aspect ratios were 1.9 ± 0.7, 3.0 ± 0.8 and 3.9 ± 0.6. Interestingly, similar size polydispersity has been found in the corresponding aspect ratio of short Au nanorods prepared by different methods.[58,61-62] **Table 2** lists the geometric parameters (mean values) and the corresponding errors. Notice that for all of the preparations, the nanorod width was ~10 nm (dispersion for the length and width values of a set of representative nanorods may be found in **Figure S3**, Supplementary Information). The mean value for nanorod length varied from 19, 27 to 39 nm with increasing [Ag^+].

Figure 10. TEM images corresponding to Au nanorods with varying aspect ratio AR, AR(a) = 1.9±0.7, AR(b) = 3.0±0.8 and AR(c) = 3.9±0.6.

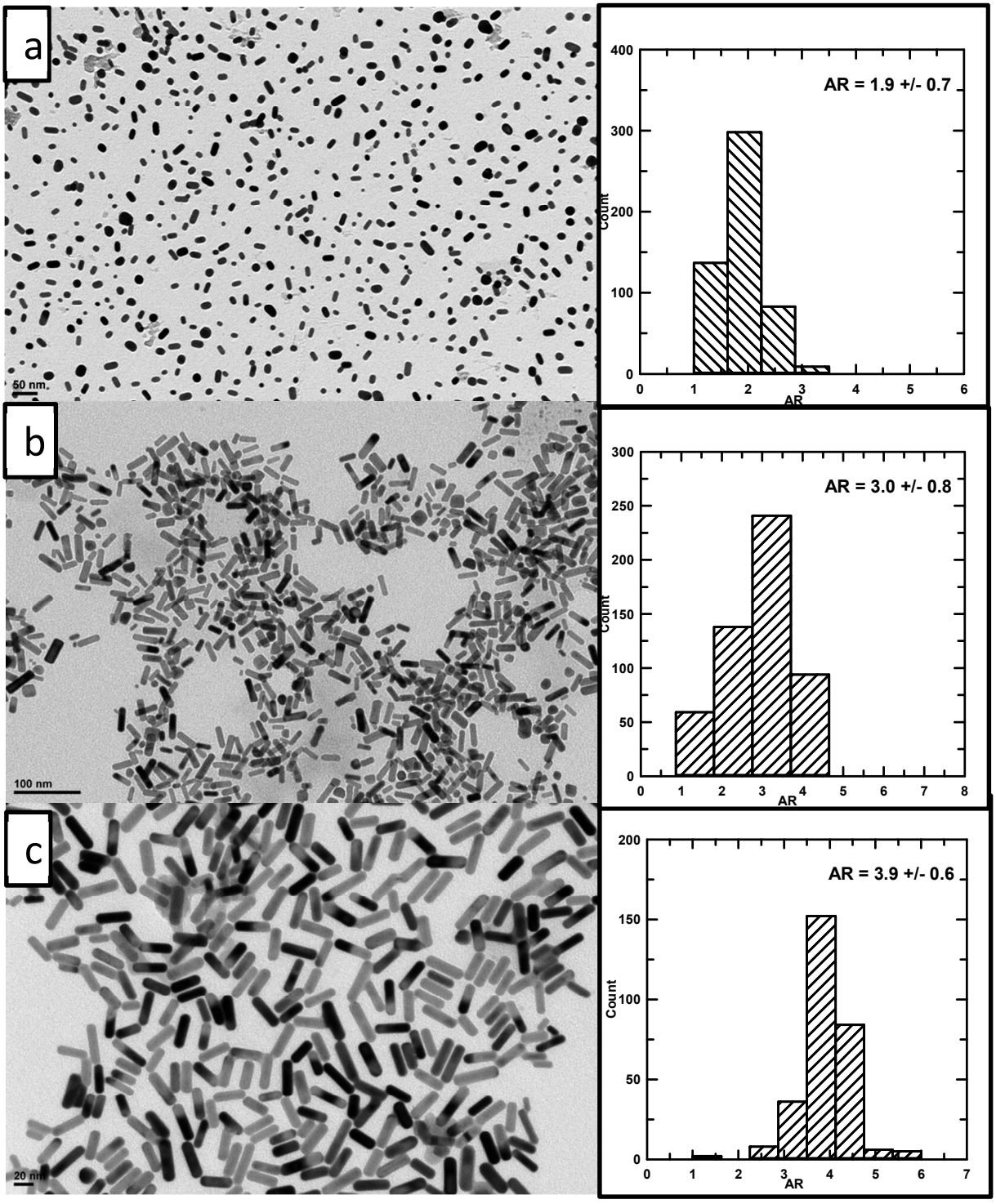

Table 2. Geometric parameters for the representative samples of Au nanorods prepared using the photochemical acetone/isopropanol system. The table lists aspect ratio (AR), nanorod length (l) and width (w) with $[Ag^+]$.

$[Ag^+]$ / μM	AR	l / nm	w / nm
30	1.9 ± 0.7	19 ± 5	10 ± 2
60	3.0 ± 0.8	27 ± 9	9 ± 3
100	3.9 ± 0.6	39 ± 7	10 ± 2

The roles of CTAB and Ag^+ in the production of Au nanorods have been profusely studied for both the photochemical and thermal routes. CTAB, acting as a soft template, is fundamental to inducing the rod shape, while Ag^+ (likely in the form of Ag bromide species, including AgBr and $AgBr_2^-$, or Ag^0) reinforces the anisotropic growth by binding specific crystallographic phases on the developing Au nanorod, and helps increase the corresponding yield.[58-60] In our experimental conditions, the production of nanorods required the use of a limiting concentration of Ag^+. In agreement with the literature, the use of increasing amounts of Ag^+ allowed the production of a range of short nanorods.[57-59,66] In absence of Ag^+, or below a threshold value (~ 30 μM for our experiments), the process yielded semi-spherical nanoparticles quantitatively. However, the highest aspect ratio accessible by this method was approximately 4 for $[Ag^+]$ = 100 μM. The use of $[Ag^+]$ > 100 μM resulted in a decrease in the yield of rod-shaped nanoparticles and an increase in the yield of spherical-like nanoparticles. This was evidenced by the relative rise of the resonance band at 520 nm. The outlined observations regarding the effect of $[Ag^+]$ on both the aspect ratio and the yield of Au nanorods agree with published experimental reports.[58-62]

In the case of the photochemical routes to Au nanorods, acetone has been found to be fundamental to accelerate the formation of Au nanorods.[56,59,61,63] It is important to note that despite this observation, such studies still reported long photolysis times (longer than 5 hours), and more intense UV irradiation levels than in our study. The role of acetone in the photochemical preparation of nanorods has not received an explanation with experimental support.[58-59,61] In fact, this was one of the reasons that

prompted us to evaluate the acetone/isopropanol system in the production of Au nanorods. It has been previously considered that the cause of the accelerating effect of acetone in the photochemical production of Au nanorods lies in the formation of reducing ketyl radicals upon electronic excitation of acetone followed by a hydrogen transfer reaction.[59-64] In such reports, CTAB has been proposed as the acting hydrogen donor (with the hydrocarbon tail supplying hydrogen atoms). This is a reasonable assumption given the well-documented reactivity of electronically excited acetone towards hydrogen donors, the well-known reducing behavior of ketyl radicals and the successful use of ketyl radicals in the photochemical preparation of group-11 metal nanoparticles (**Sections 3.2**-**3.3**).[7,37,58] Hence, comparing previous results with our own, the slow kinetics reported in the photochemical routes previously mentioned is likely related to the lack of a suitable hydrogen donor in the reaction media. In our experimental conditions, the faster rate of formation of Au nanorods is directly related to the presence of isopropanol, which is an excellent hydrogen donor.[38] This allowed the prompt formation of reducing ketyl radicals (**Equation 2**). To validate this statement, the photolysis (90 minutes) of an aqueous solution of 0.5 mM $NaAuCl_4$ in absence of isopropanol was carried out ([CTAB] = 0.1 M, [acetone] = 20 mM and $[Ag^+]$ = 60 μM). As expected, the process did not result in the formation of nanoparticulate Au during the allowed irradiation time, whereas in the presence of isopropanol, the photolysis rapidly produced nanoparticulate material after the lapse of 10 minutes, and was completed in approximately 30 minutes.

In this regard, the optimization of the concentration of acetone was critical to the formation of rod-shaped nanoparticles in a quantitative yield. In our experimental conditions, the use of acetone above a limiting concentration (20 mM) resulted in a reduction of nanorod yield and an increase in the yield of spherical-like nanoparticles. The latter was evidenced by an increase in the relative intensity of the absorption band at 520 nm. Based on the fact that the concentration of acetone used in published reports spans from 0 to 0.5 M, the limiting concentration of acetone required to produce rod-shaped nanoparticles in our experimental conditions (with a fixed UV intensity in the 250 fc range) could be related to the nucleation range afforded at the early photolysis times in this particular reaction setting.[61] In the case of the formation of colloids by

chemical routes, the nucleation phase is defined at the earliest stages of the process (supersaturation → nucleation → growth).[65] The increasing formation of spherical nanoparticles above a limiting concentration of acetone could be linked to the higher supersaturation level (seeding stage) promoted by an excess of ketyl radicals. This prospect requires the fast formation of nanoparticles to reduce the energy of the system (accelerating the growth stage), and the further distribution of the available material among a higher number of nuclei, which impends the anisotropic supply of building blocks required for nanorod growth. The latter is supported by the observed increasing yield of sphere-like nanoparticles promoted by a surplus of acetone/isopropanol. In addition, the optimal concentration of acetone/isopropanol possibly allowed the slow progression of nanoparticle shape from sphere-like seeds to rod structures because, in this situation, the operation of more complex assembly and transport mechanisms is given the opportunity to proceed in a sequence responsible for the anisotropic growth, *e.g.* ligand exchanges, surface chemistry, transport through micellar assemblies, columbic interactions.[60,66-67]

Our findings indicate that the photochemical production of Au nanorods using the acetone/isopropanol system proceeds by means of a series of steps similar to those operating in well-established thermal routes. The method offers advantages to nanorod preparation, *e.g.* fast kinetics, easy set-up, simplicity, lower cost, and can be logically extended to the preparation of nanorods with higher aspect ratio by the simple use of a cosurfactant.[60]

4. Conclusions

Our results support the advantageous use of the acetone/isopropanol system in the photochemical preparation of complex nanoparticulate systems. This study shows an example of the fine-tuning of nanoparticle morphology and the corresponding optical properties by simply adjusting reagent concentrations and light intensity. In particular, this work outlines the preparation of both AuAg alloys and core-shell nanoparticles of various compositions by the control of the irradiation source. It was found that higher UV radiation intensity promoted the formation of AuAg alloys, whereas the use of a lower UV intensity allowed the production of a core-shell structure. The prompt photochemical preparation of Au nanorods with varying aspect ratio was made possible by the

adjustment of reagent concentration, specifically the concentration of acetone/isopropanol and Ag^+.

The merits of this methodology lie in the versatility (*e.g.* production of bimetallic structures, including core-shell and alloys, and anisotropic nanoparticles), simplicity (including the 1-step process, reproducibility, the absence of organic byproducts, and well-established chemistry), and the low cost of the process (in terms of reducing agents). The process has the additional advantages of the reforming of acetone and the low toxicity profile of both acetone and isopropanol. It is also important to mention that the irradiation level employed in the outlined experiment was not particularly intense, as it is comparable to the radiance originating in a regular 100-110 V fluorescent lamp (300 fc).

Acknowledgements

We thank the National Science Foundation (PREM Center for Interfaces, DMR-1205670) for the financial support of this research. We acknowledge the support of the National Science Foundation for X-ray (Grant CRIF: MU-0946998), SEM and TEM (National Science Foundation, DUE-9052039) instrumentation, and the patronage of the Wells Foundation (AI-0045).

We also want to thank Professor William Brittain for the generous provision of laboratory space, instruments, and logistics support.

Bibliography

1. Major, K. J.; De, C.; Obare, S. O. *Plasmonics*, **2009**, *4*, 61–78.
2. Hostetler, M. J.; Zhong, Ch.-J.; Yen, B. K. H.; Anderegg, J.; Gross, S. M.; Evans, N. D.; Porter, M.; Murray, R. W. *J. Am. Chem. Soc.* **1998**, *120*, 9396-9397.
3. Anker, J. N.; Hall, W. P.; Lyandres, O.; Shah, N. C.; Zhao, J.; Van Duyne, R. P.; *Nature Materials*. **2008**, *7*, 442-453.
4. Zamborini, F. P.; Bao, L.; Radhika, D. *Anal. Chem.* **2012**, *84*, 541−576.
5. S. Link, Z. L. Wang, M. A. El-Sayed.. *J. Phys. Chem. B* **1999**, *103,* 3529-3533.
6. Moskovits, M.; Srnová-Šloufová, I.; Vlková, B. *J. Chem. Phys.* **2002,** *116*, 10435.
7. Gonzalez, C. M.; Liu, Y.; Scaiano, J. C. *J. Phys. Chem. C.* **2009,** *113,* 11861.

8. Stranik, O.; McEvoy, H.M.; McDonagh, C.; MacCraith, B.D. *Sens. and Actuators B* **2005**, *107*, 148–153.

9. Wabuyele M.; Vo-Dinh, T. *Anal. Chem.*, **2005**, *77*, 7810–7815.

10. Wang, Y.; Chen, H.; Dong, S.; Wang, E. *J. Chem. Phys.* **2006**, *125*, 044710

11. Ong, B. H.; Yuan, X. C.; Tan, Y. Y.; Irawan, R.; Fang, X. Q.; Zhang, L. S.; Tjin, S. C. *Lab Chip* **2007,** *7*, 506–512.

12. Njoki, P. N.; Wu, W.; Lutz, P.; Maye. M. M. *Chem. Mater*. **2013**, *25*, 3105−3113.

13. Cuevas-Muiz, F. M.; Guerra-Balcázar, M.; Castaneda, F.; Ledesma-García, J.; Arriaga, L. G. J. *Power Sources* **2011**, *196*, 5853−5857.

14. Lu, J.; Low, K.-B.; Lei, Y., Libera, J. A.; Nicholls, A.; Stair, P. C.; Elam, J. W. *Nat. Commun.* **2014**, 5:3264, doi: 10.1038/ncomms4264 .

15. Tsukamoto, D.; Shiro, A.; Shiraishi, Y.; Sugano, Y.; Ichikawa, S.; Tanaka, S.; Hirai, T. *ACS Catal.* **2012**, *2*, 599−603.

16. Ma, Z.; Dai, S. *ACS Catal.* **2011**, *1*, 805–818.

17. Lu, P.; Teranishi, T.; Asakura, K.; Miyake, M.; Toshima, N. *J. Phys. Chem. B* **1999**, *103*, 9673-9682 .18.

18. Suntivich, J.; Xu, Z.; Carlton, C. E.; Kim, J.; Han, B.; Lee, S. W.; Bonnet, N.; Marzari, N.; Allard, L. F.; Gasteiger, H. A.; Hamad-Schifferli, K.; Shao-Horn, Y. *J. Am. Chem. Soc.* **2013**, *135*, 7985−7991.

19. Zhang, H.; Haba, M.; Okumura, M.; Akita, T.; Hashimoto, S.; Toshima, N. *Langmuir* **2013**, *29*, 10330−10339.

20. Menezes, W. G.; Neumann, B.; Zielasek, V.; Thiel, K.; Bäumer, M. *ChemPhysChem* **2013**, *14*, 1577–1581.

21. Kale, M. J.; Avanesian, T.; Christopher, P. A*CS Catal.* **2014**, *4*, 116−128.

22. Hartland, G. V. *Chem. Rev*. **2011**, *111*, 3858–3887.

23. Walker, J. M.; Gou, Li. Bhattacharyya, S.; Lindahl, S. E.; Zaleski, J. M. *Chem. Mater*. **2011**, *23*, 5275−5281.

24. Wurtz, G. A.; Evans, P. R.; Hendren, W.; Atkinson, R.; Dickson, W.; Pollard, R. J.; Zayats A. V.**.** *Nano Lett.* **2007,** *7*, 1297–*1303***.**

25. Link, S.; El-Sayed, M.A. *J. Phys. Chem. B* **1999**, *103*, 8410–8426.

26. Sharma , V.; Park, K.; Srinivasarao, M. *Materials Science and Engineering R* **2009**, *65*, 1–38.
27. Alkilany, A. M.; Thompson, L. B.; Boulos, S. P.; Sisco, P.N. Murphy, C. J. *Advanced Drug Delivery Reviews* **2012,** *64*, 190–199.
28. Huang, X.; El-Sayed, I. H.; Qian, W.; El-Sayed, M. A. *J. Am. Chem. Soc.* **2006**, *128*, 2115–2120.
29. Orendorff, C. J.; Gole, A.; Sau, T. K.; Murphy, C. J. A*nal. Chem*. **2005,** *77*, 3261–3266.
30. Bardhan, R.; Grady, N. K.; Cole, J. R.; Joshi, A.; Halas, N. J. *ACS Nano***. 2009,** *3,* 744–752**.**
31. Kumar, J. K.; Thomas, G. K. *J. Phys. Chem. Lett.* **2011**, *2*, 610–615.
32. Crawley, N.; Thompson, M. *Anal. Chem.* **2014**, *86*, 130−160.
33. Mayer, K. M.; Hafner, J. H. *Chem. Rev.* **2011**, *111*, 3828–3857.
34. Wang, Z. L.; Mohamed, M. B.; Link, S.; El-Sayed, M. A. *Surf. Sci.* **1999**, *440*, L809–L814.
35. Jana, N. R.; Gearheart, L.; Obare, S. O.; Murphy, C. J. *Langmuir* **2002**, *18,* 922–927.
36. Wang, Z. L.; Gao, R. P.; Nikoobakht, B.; El-Sayed, M. A. *J. Phys. Chem. B* **2000**, *104*, 5417–5420
37. Kasama, K.; Takematsu, A.; Aral, S. *J. Phys Chem*. **1982**, *86*, 2420.
38. Turro, N. J. *Modern Molecular Photochemistry*. University Science Books: Sausalito, California, **1991**.
39. Grotewold, J.; Soria, D.; Previtali, C. M.; Scaiano, J. C. *J. Photochem*. **1972–1973**, *1*, 471.
40. Laroff, G. P.; Fisher, H. *Helv. Chem. Acta.* **1973**, *45*, 506.
41. Zeldes, H.; Livingston, R. *J. Chem. Phys*. **1966**, *45*, 1946.
42. Nakashima, M.; Hayon. E. *J. Phys Chem*. **1971***, 75*, 1910.
43. Scaiano, J. C.; Billone, P.; Gonzalez, C.M.; Maretti, L.; Marin, M. L.; McGilvray, K. L.; Yuan. N. *Pure Appl. Chem.* **2009**, 81, *635*.
44. Treguer, M.; de Cointet, C.; Remita, H.; Khatouri, J.; Mostafavi, M.; Amblard, J.; Belloni, J. *J. Phys. Chem. B* **1998,** *102,* 4310–4321.

45. Verbruggen, S. W.; Keulemans, M.; Martens, J. A.; Lenaerts, S. *J. Phys. Chem. C* **2013**, *117*, 19142−19145.
46. Eustis, S.; Hsu, H.-Y.; El-Sayed, M. A. *J. Phys. Chem. B*. **2005**, *109*, 4811.
47. Eustis, S.; El-Sayed, M. A. *J. Phys. Chem. B*. **2006**, *110*, 14014.
48. Hodak, J. H.; Henglein, A.; Hartland, G. V. *J. Phys. Chem. B* **2000,** *104,* 9954.
49. Henglein, A.; Lilie, J. *J . Am. Chem. Soc*. **1981**, *103*, 1059.
50. Subramanian, V.; Wolf, E. E.; Kamat, P. V. *J. Phys. Chem. B* **2003,** *107,* 7479–7485.
51. DeSantis, C. J.; Weiner, R. G.; Radmilovic, A.;. Bower, M. M.; Skrabalak, S. E. *J. Phys. Chem. Lett.* **2013**, *4*, 3072−3082.
52. Abid, J.-P.; Nappa, J.;. Girault, H. H.; Brevet, P.-F. *J. Chem. Phys*., **2004**, *121*, 12577–12582.
53. Hodak, J. H.; Henglein, A.; Giersig, M.; Hartland, G. V. *J. Phys. Chem. B* **2000,** *104,* 11708–11718.
54. Chen, Y.; Wu, H.; Li, Z.; Wang, P.; Yang, L.; Fang, Y. *Plasmonics* **2012**, *7*, 509–513
55. Morriss, R. H.; Collins, L. F. *J. Chem. Phys***. 1964,** *41*, 3357–3363**.**
56. Kim, F.; Song, J. H.; Yang, P. *J . Am. Chem. Soc*.**, 2002,** *124*, 14316–14317.
57. Nikoobakht, B.; El-Sayed, M. A. *Chem. Mater.* **2003,** *15,* 1957–1962.
58. Ahmed, M.; Narain, R. *Langmuir* **2010**, *26*, 18392–18399.
59. Placido, T.; Comparelli, R.; Giannici, F.; Cozzoli, P. D.; Capitani, G.; Striccoli, M.; Agostiano, A.; Curri, M. L. *Langmuir* **2002,** *18,* 922–927.
60. Lohse, S. E.; Murphy, C. J. *Chem. Mater.* **2013**, *25*, 1250−1261.
61. Miranda, O. R.; Ahmadi, T. S. *J. Phys. Chem. B* **2005,** *109,* 15724–15734.
62. Garg, N.; Scholl, C.; Mohanty, A.; Jin, R. *Langmuir* **2010**, *26,* 10271–10276.
63. Esumi, K.; Matsuhisa, K.; Torigoe, K. *Langmuir* **1995**,*11*, 3285–3287.
64. Nishioka, K.; Niidome, Y.; Yamada, S. *Langmuir* **2007,** *23,* 10353–10356.
65. Burda, C.; Chen, X.; Narayanan, R.; El-Sayed, M. A. *Chem. Rev.* **2005,** *105*, 1025–1102.
66. Sau, T. K.; Murphy, C. J. *Langmuir* **2004,** *20,* 6414–6420
67. Gole, A.; Murphy, C. J. *Chem. Mater.* **2004,** *16,* 3633–3640.

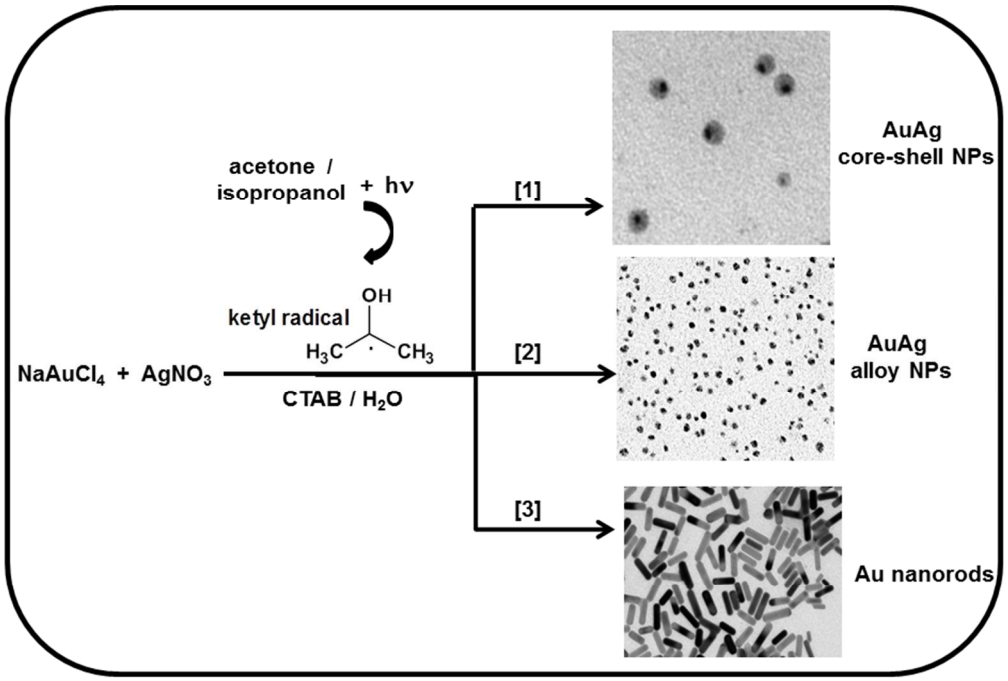

248x167mm (96 x 96 DPI)